Magnetic Field Solution in Doubly-Slotted Airgap of Conventional and Alternate Field-Excited Switched-Flux Topologies

Benjamin Gaussens, Emmanuel Hoang, Olivier de La Barrière, J. Saint Michel, Michel Lécrivain, Mohamed Gabsi

Magnetic Field Solution in Doubly-Slotted Airgap of Conventional and Alternate Field-Excited Switched-Flux Topologies

Benjamin Gaussens[12], *Student Member, IEEE,* Olivier de la Barrière[1], Emmanuel Hoang[1], Jacques Saint-Michel[2], Philippe Manfe[2], Michel Lécrivain[1], and Mohamed Gabsi[1], *Member, IEEE*

[1] SATIE, ENS Cachan, CNRS, UniverSud, 61 av. du President Wilson, Cachan F-94230, France
[2]Leroy Somer, Emerson, EPG Division, Sillac, Bd Marcellin Leroy - 16015 Angoulême Cedex, France

A general solution of the magnetic field in the airgap of Conventional and Alternate Field-Excited Switched-Flux (FE-SF) machines is proposed in this paper. The analytical model is based on subdomain method. It involves solution of governing field equations in a doubly-slotted airgap using the variable separation method. The complete model is derived and described in a general manner so that it can be easily extended to unconventional FE-SF topologies. By means of example, analytical predictions of airgap field are extensively compared and validated using 2D FE results. FE simulations were performed on a 24-10 classical FE-SF structure and also, on a novel 18-11 FE-SF machine with additional spacer teeth.

***Index Terms*—Exact analytical calculation, flux-switching, switched-flux, slotting effect, Poisson Laplace's equation.**

I. Introduction

PRINCIPLE of flux-switching can be tracked back in the 50's and was originally validated on a single-phase flux-switching alternator [1]. Over the last decade, there has been an increasing interest in Flux-Switching, also named Switched-Flux (SF) machines, particularly Permanent Magnet-excited (PM-SF) polyphased topologies [2][3]. Since then, suitability of SF-PM machines for various applications has been confirmed by the considerable amount of work carried out by researchers, particularly in United-kingdom[4][5][6], China [7][8][9], France [10][11][12] and Japan [13].

Switched-flux machines have bipolar phase flux-linkage waveform resulting in a sinusoidal-like back-electromotive force (EMF), despite their doubly-slotted airgap. Moreover, during the design stage, the back-EMF can be optimized to reduce its harmonic content since it strongly depends on stator and rotor relative slot opening. It worth mentioning their rugged structure, with a passive rotor similar to that of Switched Reluctance machines, and suitable for high-speed operation. In addition, all active parts (concentrated phase windings and PM) are housed in the stator allowing brushless operations with reduced maintenance and eased cooling. For all these reasons, SF-PM appears to be eligible for many industrial applications that are increasingly demanding for electromagnetic devices combining high torque density, high efficiency and robustness.

However, the constant field provided by magnets in PM-SF structures was not in accordance with requirements of variable speed applications, notably a good field-weakening capability. Hence, Hybrid-Excited Switched-Flux (HE-SF) machines were proposed. Those topologies combine both PM and an additional DC winding fluxes to achieve a good flux control capability. The wealth of literature on HE-SF machines can be sorted into two groups, i.e. series flux path [14][15] or parallels flux path [16] HE-FS machines, depending on DC coils location and the flux control principle. It worth mentioning the recent work [17], where a novel HE-FS topology with excitation coils located in stator slots is presented. Its innovative flux control principle is explained and further validated with experiments. Authors showed, trough Finite Element (FE) simulations, that this topology belongs to both series and parallels flux path HE-SF machines, depending on the rotor teeth number.

Recent published works have unlocked new avenues and show interesting prospects for the future of HE-SF topologies, especially for applications requiring extended constant power operation range with improved efficiency [10][18]. Nevertheless, risks of supply-chain disruptions for some rare earth materials in short-term led governments, industrial organizations and researchers to rethink their approach.

The Field-Excited Switched-Flux (FE-SF) machine may be a prime candidate to overcome those risks. So far, despite a general agreement on their attractive low-cost topology, FE-SF topology has been much less investigated than the corresponding PM-SF machine. To the author's knowledge, just two topologies of FE-FS machines are mentioned in literature, while numerous new PM-excited topologies have been developed, as highlighted in [4]. Classical FE-SF structures with overlapping windings are investigated in [19][20], while a modular rotor topology with non-overlapping windings is presented in [21].

Generally, Finite Elements methods are preferred to assess electromagnetic performances of FS machines. Indeed, their complex structure with a doubly-slotted airgap, together with high-flux focusing effect, mainly in PM-SF machines, may require accounting for the non-linear behavior of magnetic material. Despite their excellent accuracy, FE simulations are severely limited by computational time requirements, and thus, exploration of various designs is directly affected. To go beyond those limitations, some authors proposed models of PM-FS and HE-FS topologies in a more analytical manner, using Magnetic Equivalent Circuit (MEC) [22][23], Fourier analysis

Manuscript received ..

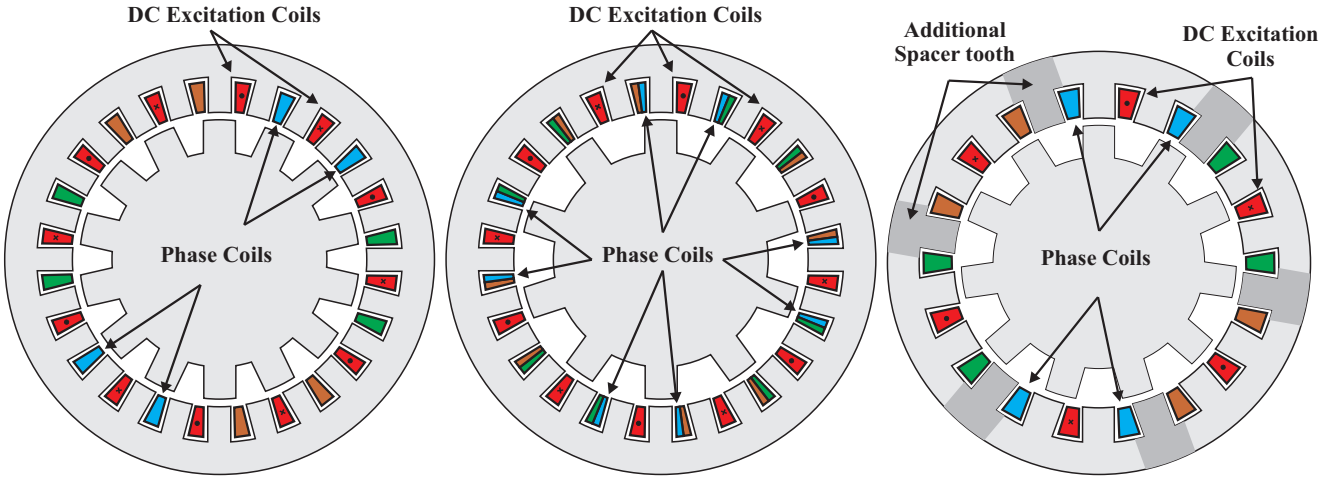

Fig. 1. Conventional and Alternate Field-Excited Switched-Flux machines: Classical FE-SF with single (a) or double-layers windings (b) and Unconventional FE-SF machine with additional spacer teeth (c)

method [24], spatial discretization methods [25] and tooth contour methods [26]. In reference [27], an analytical model for classical FE-SF machines based on Magnetomotive Force-Permeance theory was proposed. This analytical field model can fairly predict the radial component of the flux-density in the airgap to determine the main performances at no-load, as flux-linkage or back-EMF. However, it neglects slots leakage, mutual influence between slots and cannot predict tangential component of magnetic field to assess the electromagnetic torque trough the Maxwell stress tensor. Moreover, this model was just bounded to classical FE-FS machines. Indeed, no references in the literature addressing the issue of an exact analytical model for both classical and alternate Field-Excited Switched-Flux machines were found, while it is of first interest to improve the analysis and the design of unconventional FE-FS machines.

Regarding modeling techniques to account for the slotting effect, two approaches are mainly reported in the literature. Some authors propose to use a relative permeance function that could modulate the airgap field calculated without slots. The permeance function can be derived using conformal transformation and considering infinitely deep slot [28][29][30][31]. Others works derive a modulating function assuming idealized flux-lines under the slot[32][33][34][35]. It was as well proposed an exact permeance function accounting for all the slot dimensions in [36]. Another approach is named subdomain model. The main idea consists in solving directly the governing field equations in different domains, and applying boundary conditions on the interfaces between subdomains [37][38][39][40][41][42]. In so doing, it is possible to derivate an exact expression of the magnetic field.

The objective of this paper is to derive an analytical solution of the magnetic field in classical and alternate Field-Excited Switched-Flux machines based on subdomain method to predict both open circuit, armature reaction and on-load field. The approach assumes that the magnetic material is linear. This article has been organized in the following way. Firstly, the classical and unconventional topologies are briefly introduced to determine a simplified geometry to model. Then, exact magnetic field solution in the doubly slotted airgap of FE-SF machines is proposed. The analytical field expression in each subdomain is derived by the variable separation method. Afterwards, boundary and interface conditions are applied to set up a system of linear equations. In the fourth section, extensive comparisons with flux-density distributions obtained by FE simulations come to validate the analytical model.

II. Conventional and Alternate FE-SF topologies

In this section, conventional and alternate Field-Excited Switched-Flux machines are introduced. Contrary to PM-excited topologies, FE-SF machines have received less attention in the research community. Classical FE-SF machines with single or double-layer windings are presented in Fig. 1.(a) and (b). It should be noted that the rotor pole number is not the same between these topologies. Indeed, in FE-SF machines, the stator-rotor teeth combination is not fixed and may create modification in windings configurations. An unconventional FE-SF machine is depicted in Fig. 1.(c). It has additional spacer teeth, highlighted in dark-grey color, linking two flux-switching cells, and single layer windings. Also, this topology has less DC excitation slots leading to reduced cost and greater efficiency, because of reduced excitation Joule losses. A similar PM-excited topology was reported in [43], however, this field-excited topology has never been published or studied to the author's knowledge.

The main idea of this work is to derive an analytical solution of the magnetic field in the doubly-slotted airgap of FE-SF machines as general as possible, and flexible enough for an eased extension to unconventional machines having static DC excitation winding. Earlier in this paragraph, we presented some conventional and alternate FE-SF machines, but the foregoing model is not restricted to these structures. For illustrative purposes, the airgap field of the topology reported in [44] could be modeled according to the subsequent analytical magnetic field solution.

III. Magnetic Field Solution in the Doubly-Slotted Airgap of FE-SF Machines

Considering the above mentioned topologies (Fig. 1), a general geometrical model is proposed in Fig. 2. As can be seen, the field domain is divided into 3 subdomains, *viz.* airgap (domain I), rotor slots (domains i) and stator slots (domains j). Stator and rotor slots opening are $\beta_s\theta_s$ and $\beta_r\theta_r$ respectively. The angular position in the airgap is defined with ν, and θ corresponds to the rotor position.

In order to derive a general analytical framework for FE-SF machines, a non overlapping winding configuration is studied, *i.e.* with two different current densities sharing the same stator slot. This will later enable to predict electromagnetic performances of single- or double-layers configurations, and then, determine field distributions of unconventional FE-SF topologies just by modifying windings (DC excitation and phase) location.

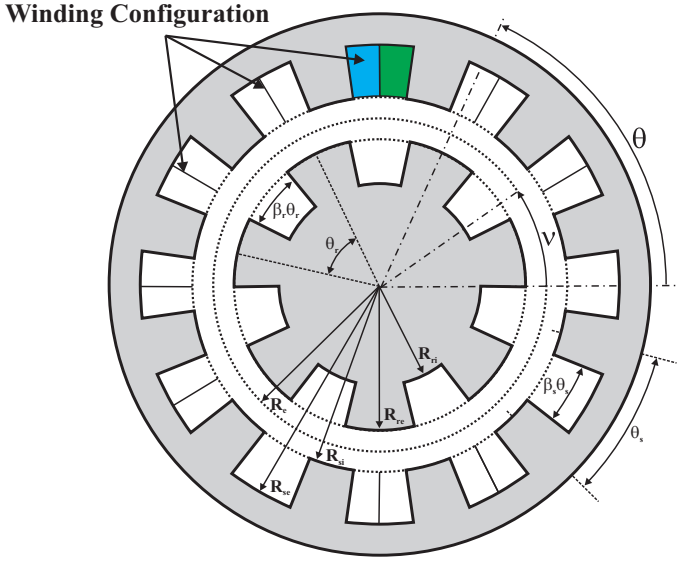

Fig. 2. Doubly-salient geometry of FS machine with $N_s = 12$ and $N_r = 7$ with its double-layer windings

Some assumptions are made in order to simplify the problem:

- Infinite permeability of rotor and stator core, hence, no-magnetic saturation of iron regions is considered.
- Non-conductive stator or rotor laminated iron sheets (No eddy currents)
- 2D problem (end effects are neglected) with a uniform current density in coil's conductor area and only one component along the z-axis.
- Stator and rotor slots have radial sides.

According to the 2D problem assumption, the magnetic vector potential $\vec{A}$ has only one component along the z-direction and only depends on r and ν coordinates.

The partial differential equations (PDE) that are governing the magnetic field behavior in a continuous/isotropic region in term of magnetic vector potential are Laplace's equations for rotor slots,

$$\Delta A_i = 0, \text{ in the } i^{\text{th}} \text{ rotor slot (Region } i) \tag{1}$$

and airgap,

$$\Delta A_I = 0, \text{ in the airgap (Region } I) \tag{2}$$

and Poisson's equation for stator slots,

$$\Delta A_j = -\mu_0 J_j, \text{ in the } j^{\text{th}} \text{ rotor slot (Region } j) \tag{3}$$

with J_q the stator slot current density and μ_0 the vacuum permeability.

A. General Solution of Laplace's Equation in Airgap (Region I)

The Laplace's equation (2) governing the field in the airgap domain, can be rewritten in polar coordinates as

$$\frac{\partial^2 A_I}{\partial r^2} + \frac{1}{r}\frac{\partial A_I}{\partial r} + \frac{1}{r^2}\frac{\partial^2 A_I}{\partial \nu^2} = 0 \text{ for } \begin{cases} r \in [R_{re}, R_{si}] \\ \nu \in [0, 2\pi] \end{cases} \tag{4}$$

with R_{re} the external radius of the rotor, R_{si} the internal radius. Also, it should be noted that the whole airgap is considered, *i.e.* over a 2π-mechanical angle. That will allow us to account for non-periodic geometries, *viz.* with $\gcd(N_s, N_r) = 1$. N_s and N_r are respectively the number of stator and rotor teeth.

The general solution of (4) can be found by separating the variable r and ν, so that the solution can be written as

$$A_I(r,\nu) = \sum_{n\geq 1}\left[A_n^{(I)}\left(\frac{r}{R_{re}}\right)^{-n} + B_n^{(I)}\left(\frac{r}{R_{si}}\right)^{n}\right]\cos(n\nu) + \left[C_n^{(I)}\left(\frac{r}{R_{re}}\right)^{-n} + D_n^{(I)}\left(\frac{r}{R_{si}}\right)^{n}\right]\sin(n\nu) \tag{5}$$

with A_n, B_n, C_n and D_n Fourier coefficients to be determined.

B. General Solution of Poisson's Equation in Stator Slots (Region j)

In each stator slots, we have to solve the Poisson's equation, defined by (3), to determine the vector-potential distribution. According to the superposition law, the general solution is the sum of the corresponding Laplace's equation (with $J_j = 0$) and a particular solution A_{j_p} of its own. As previously, assuming a polar coordinate system, equation (3) becomes,

$$\frac{\partial^2 A_j}{\partial r^2} + \frac{1}{r}\frac{\partial A_j}{\partial r} + \frac{1}{r^2}\frac{\partial^2 A_j}{\partial \nu^2} = -\mu_0 J_j \text{ for } \begin{cases} r \in [R_{si}, R_{se}] \\ \nu \in \left[\theta_j, \theta_j + \beta_{s_j}\theta_s\right] \end{cases} \tag{6}$$

We first consider the solution of the corresponding Laplace's equation. Fig. 3 presents the slotted stator geometry with the associated boundary conditions. Since stator core is assumed to be highly permeable, Neumann boundary conditions are considered respectively on each tooth sides and at the bottom

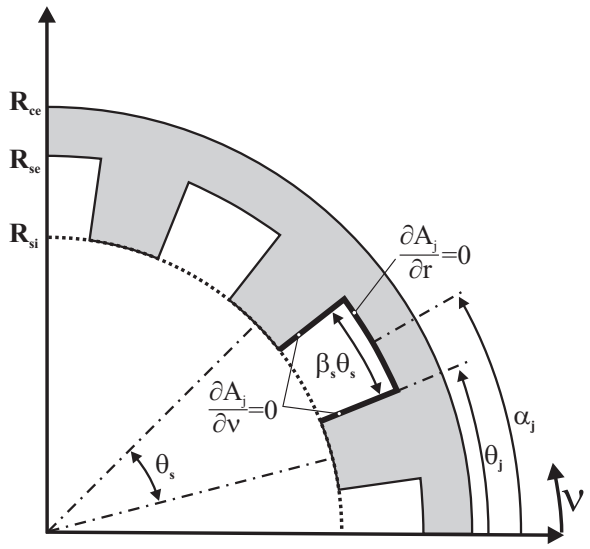

Fig. 3. Slotted stator geometry with associated boundary conditions

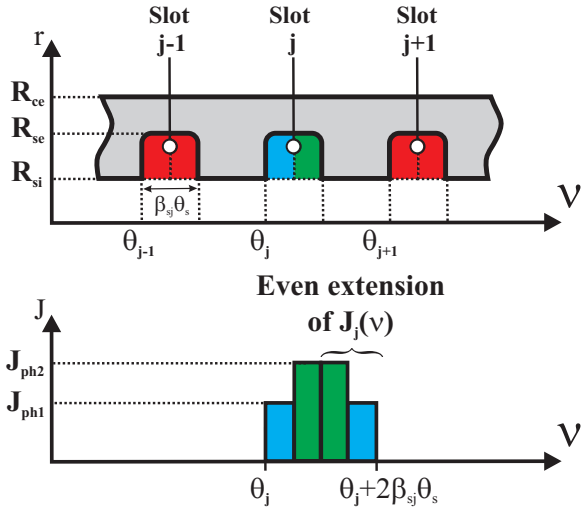

Fig. 4. Current density distribution in the non-overlapping double-layer stator slot - Even extension of the current density $J_j(\nu)$ using the image method

of the slot. Finally, the j^{th} stator slot is associated with the following boundary conditions,

$$\frac{\partial A_j\left(r,\nu=\alpha_j\pm\frac{\beta_{s_j}\theta_s}{2}\right)}{\partial\nu}=0 \text{ for } r\in[R_{si},R_{se}] \quad (7)$$

and

$$\frac{\partial A_j\left(r=R_{se},\nu\right)}{\partial r}=0 \text{ for } \nu\in\left[\theta_j,\theta_j+\beta_{s_j}\theta_s\right] \quad (8)$$

To satisfy boundary conditions (8) and assuming a solution with separated variables, it is possible to express the vector-potential A_j as,

$$A_j\left(r,\nu\right)=A_0^{(j)}+B_0^{(j)}\ln\left(r\right)+\sum_{q\geq1}\left[A_q^{(j)}r^{-q\frac{\pi}{\beta_{s_j}\theta_s}}+B_q^{(j)}r^{q\frac{\pi}{\beta_{s_j}\theta_s}}\right]\cos\left(q\frac{\pi}{\beta_{s_j}\theta_s}\left(\nu-\theta_j\right)\right) \quad (9)$$

where R_{se} the radius of the slot bottom and $A_0^{(j)}$, $B_0^{(j)}$, $A_q^{(j)}$ and $B_q^{(j)}$ coefficients to be determined.

We now have to determine a particular solution of (6). To do so, we first consider the non-overlapping winding depicted in Fig. 4. Since the current density is uniform over each coil, the current density distribution J_q is radius-independent, and can be defined by a function by parts over $[\theta_j,\theta_j+2\beta_{s_j}\theta_s]$ intervals as shown in Fig. 4,

$$J_j(\nu)=\begin{cases}J_{ph_1} & ,\forall\nu\in\left[\theta_j,\theta_j+\frac{\beta_{s_j}\theta_s}{2}\right]\\ J_{ph_2} & ,\forall\nu\in\left[\theta_j+\frac{\beta_{s_j}\theta_s}{2},\theta_j+\beta_{s_j}\theta_s\right]\end{cases} \quad (10)$$

Expanding (10) into Fourier series over $[\theta_j,\theta_j+2\beta_{s_j}\theta_s]$, it yields to,

$$J_j(\nu)=J_{j_0}+\sum_{q\geq1}J_{jq}\cos\left(q\frac{\pi}{\beta_{s_j}\theta_s}\left(\nu-\theta_j\right)\right) \text{ for } \nu\in\left[\theta_j,\theta_j+\beta_{s_j}\theta_s\right] \quad (11)$$

with the mean value,

$$J_{j_0}=\frac{J_{ph_1}+J_{ph_2}}{2} \quad (12)$$

and the following Fourier serie coefficients,

$$J_{jq}=\frac{2}{T}\int_{\theta_j}^{2\beta_{s_j}\theta_s+\theta_j}J_j\left(\nu\right)\cos\left(q\frac{\pi}{\beta_{s_j}\theta_s}\nu\right)d\nu=\frac{2\left(J_{ph1}-J_{ph_2}\right)}{q\pi}\sin\left(q\frac{\pi}{2}\right) \quad (13)$$

Considering the form of the current density distribution (See Eq. (11)), a particular solution A_{j_p} can be found as,

$$A_{j_p}(\nu)=-\mu_0\frac{J_{j0}}{4}r^2-\sum_{q\geq1}\mu_o\frac{J_{jq}}{4-\left(q\frac{\pi}{\beta_{s_j}\theta_s}\right)^2}r^2\cos\left(q\frac{\pi}{\beta_{s_j}\theta_s}\left(\nu-\theta_j\right)\right) \quad (14)$$

Therefore, the vector-potential A_j in the jth slot can be expressed as,

$$A_j\left(r,\nu\right)=A_0^{(j)}+B_0^{(j)}\ln\left(r\right)-\mu_0\frac{J_{j0}}{4}r^2+\sum_{q\geq1}\left[A_q^{(j)}r^{-q\frac{\pi}{\beta_{s_j}\theta_s}}+B_q^{(j)}r^{q\frac{\pi}{\beta_{s_j}\theta_s}}-\mu_o\frac{J_{jq}}{4-\left(q\frac{\pi}{\beta_{s_j}\theta_s}\right)^2}r^2\right]\cos\left(q\frac{\pi}{\beta_{s_j}\theta_s}\left(\nu-\theta_j\right)\right) \quad (15)$$

Accordingly to the Neumann boundary condition at the slot bottom, defined by (7), the number of unknown independent coefficients can be reduced,

$$B_0^{(j)} = \mu_0 \frac{J_{j0}}{2} R_{se}^2 \tag{16}$$

and

$$B_q^{(j)} = A_q^{(j)} R_{se}^{-2q\frac{\pi}{\beta_{s_j}\theta_s}} + 2\mu_o \frac{J_{jq}}{\left(4 - \left(q\frac{\pi}{\beta_{s_j}\theta_s}\right)^2\right)\left(q\frac{\pi}{\beta_{s_j}\theta_s}\right)} R_{se}^{-q\frac{\pi}{\beta_{s_j}\theta_s}+2} \tag{17}$$

Finally, from (15), (16) and (17), the general solution of the vector-potential A_j in the jth slot can be derived as

$$A_j(r,\nu) = A_0^{(j)} + \mu_0 \frac{J_{j0}}{2}\left(R_{se}^2 \ln(r) - \frac{r^2}{2}\right) + \sum_{q\geq 1}\left[A_q^{(j)}\left[\left(\frac{r}{R_{si}}\right)^{-q\frac{\pi}{\beta_{s_j}\theta_s}} + \beta_1\left(\frac{r}{R_{se}}\right)^{q\frac{\pi}{\beta_{s_j}\theta_s}}\right] - \mu_o \frac{J_{jq}}{4-\left(q\frac{\pi}{\beta_{s_j}\theta_s}\right)^2}\left(r^2 - \frac{2R_{se}^2}{\left(q\frac{\pi}{\beta_{s_j}\theta_s}\right)}\left(\frac{r}{R_{se}}\right)^{q\frac{\pi}{\beta_{s_j}\theta_s}}\right)\right] \cos\left(q\frac{\pi}{\beta_{s_j}\theta_s}(\nu-\theta_j)\right) \tag{18}$$

with

$$\beta_1 = \left(\frac{R_{si}}{R_{se}}\right)^{q\frac{\pi}{\beta_{s_j}\theta_s}} \tag{19}$$

$A_0^{(j)}$ and $A_q^{(j)}$ are coefficients to be determined later.

C. General Solution of Laplace's Equation in Rotor Slots (Region i)

The field behavior in the ith rotor slot is governed by the following Laplace's equation,

$$\frac{\partial^2 A_i}{\partial r^2} + \frac{1}{r}\frac{\partial A_i}{\partial r} + \frac{1}{r^2}\frac{\partial^2 A_i}{\partial \nu^2} = 0 \text{ pour } \begin{cases} r \in [R_{ri}, R_{re}] \\ \nu \in [\theta_i, \theta_i + \beta_{r_i}\theta_r] \end{cases} \tag{20}$$

in polar coordinates. R_{ri} is the radius of the rotor slot bottom.

In Fig. 5 an idealized rotor slot geometry is presented. As previously, interfaces between air and an highly permeable iron lead again to Neumann boundary conditions,

$$\frac{\partial A_i\left(r, \nu = \alpha_i \pm \frac{\beta_{r_i}\theta_r}{2}\right)}{\partial \nu} = 0 \text{ for } r \in [R_{ri}, R_{re}] \tag{21}$$

for each rotor tooth sides, and

$$\frac{\partial A_i(r = R_{ri}, \nu)}{\partial r} = 0 \text{ for } \nu \in [\theta_i, \theta_i + \beta_{r_i}\theta_r] \tag{22}$$

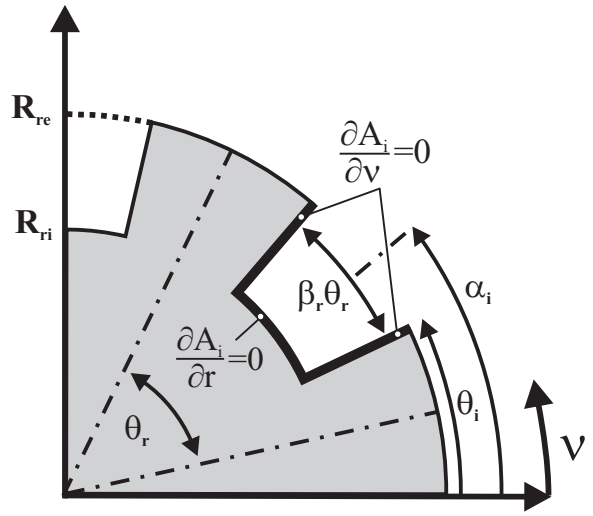

Fig. 5. Slotted rotor geometry with associated boundary conditions

for the rotor slot bottom, and where $\theta_i = \alpha_i + \theta$ with $\alpha_i = \theta_r\left(1 - \frac{\beta_{r_i}}{2}\right)$. Considering the Neumann boundary condition (21), it is possible to look into solution of the form,

$$A_i(r,\nu) = A_0^{(i)} + B_0^{(i)}\ln(r) + \sum_{k\geq 1}\left[A_k^{(i)} r^{-k\frac{\pi}{\beta_{r_i}\theta_r}} + B_k^{(i)} r^{k\frac{\pi}{\beta_{r_i}\theta_r}}\right]\cos\left(k\frac{\pi}{\beta_{r_i}\theta_r}(\nu-\theta_i)\right) \tag{23}$$

The second boundary condition, defined by (22), helps us to determine some unknown coefficients, so that, the general expression of vector-potential A_i in the ith slot can be expressed as,

$$A_i(r,\nu) = A_0^{(i)} + \sum_{k\geq 1} A_k^{(i)} \left[\beta_2\left(\frac{r}{R_{ri}}\right)^{-k\frac{\pi}{\beta_{r_i}\theta_r}} + \left(\frac{r}{R_{re}}\right)^{k\frac{\pi}{\beta_{r_i}\theta_r}}\right]\cos\left(k\frac{\pi}{\beta_{r_i}\theta_r}(\nu-\theta_i)\right) \tag{24}$$

with

$$\beta_2 = \left(\frac{R_{re}}{R_{ri}}\right)^{-k\frac{\pi}{\beta_{r_i}\theta_r}} \tag{25}$$

The constant terms $A_0^{(i)}$ and $A_k^{(i)}$ are coefficients to be determined.

D. Boundary and Interface Conditions

Now that general expressions of vector-potential in each subdomain have been derived, we need to apply boundary and interface conditions to determine the unknown coefficients A_n, B_n, C_n, D_n, $A_0^{(i)}$, $A_k^{(i)}$, $A_0^{(j)}$ and $A_q^{(j)}$.

Basically, interface conditions between two subdomains in term of vector-potential have to ensure,

- the continuity of vector-potential ;

- the continuity of the normal derivative of vector-potential, equivalent to the continuity of the tangential magnetic field since both stator slots, airgap region and rotor slots have the same magnetic permeability μ_r.

To this end, the boundary integral method is applied to this problem and detailled in the following paragraphs.

1) Continuity of the Normal Derivative of Vector-potential

As specified beforehand, the normal derivative of the vector-potential has to be continuous between each subdomain. However, because of slotted stator and rotor, ensuring this condition requires some analytical developments.

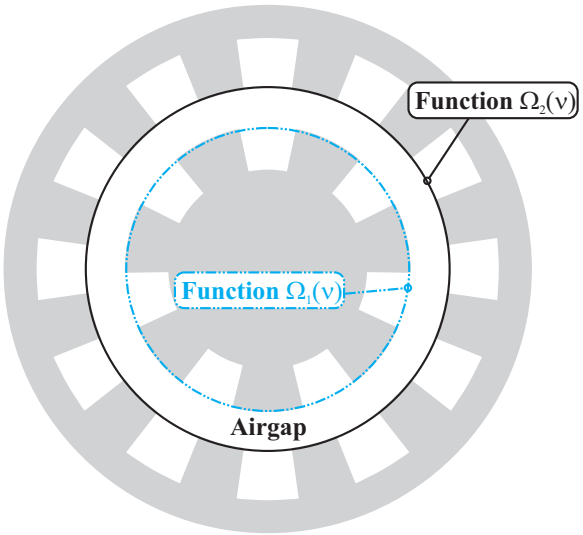

Fig. 6. Shematic representation of airgap domain surrounded by stator and rotor cores - Definition of functions $\Omega_1(\nu)$ and $\Omega_2(\nu)$ to ensure the continuity of the normal derivative of vector-potential between airgap domain and respectively the rotor (blue dotted lines) and the stator (black solid lines)

A shematic representation of the airgap domain, surrounded by stator or rotor teeth, is proposed Fig. 6. When the airgap is facing a tooth - (stator or rotor), the infinite permeability of core allows us to consider that the normal derivative of vector-potential in the airgap is null. Elsewhere, the airgap vector-potential normal derivative should equal either stator or rotor slots normal derivative of vector-potential. Finally, it can be written that,

$$\left.\frac{\partial A_I(r,\nu)}{\partial r}\right|_{r=R_{re}} = \Omega_1(\nu) = \begin{cases} \left.\frac{\partial A_i(r,\nu)}{\partial r}\right|_{r=R_{re}} & \text{for } \nu \in [\theta_i, \theta_i+\beta_{r_i}\theta_r] \\ 0 & \text{elsewhere} \end{cases} \quad (26)$$

at the airgap internal radius $r = R_{re}$, *i.e.* airgap-rotor interface, and,

$$\left.\frac{\partial A_I(r,\nu)}{\partial r}\right|_{r=R_{si}} = \Omega_2(\nu) = \begin{cases} \left.\frac{\partial A_j(r,\nu)}{\partial r}\right|_{r=R_{si}} & \text{for } \nu \in [\theta_j, \theta_j+\beta_{s_j}\theta_s] \\ 0 & \text{elsewhere} \end{cases} \quad (27)$$

at the airgap external radius $r = R_{si}$, *i.e.* airgap-stator interface. It should be noted that two functions, respectively $\Omega_1(\nu)$ and $\Omega_2(\nu)$, are introduced. They refer to Fourier series expansions over the whole airgap, *i.e.* over $[0, 2\pi]$, of conditions (26) and (27).

First of all, from (24), the normal derivative of vector-potential in the ith slot at the airgap-rotor interface ($r = R_{re}$) is found to be,

$$\left.\frac{\partial A_i(r,\nu)}{\partial r}\right|_{r=R_{re}} = \sum_{k\geq 1} A_k^{(i)} \Lambda_{1ki} \cos\left(k\frac{\pi}{\beta_{r_i}\theta_r}(\nu-\theta_i)\right) \quad (28)$$

with

$$\Lambda_{1ki} = \left(k\frac{\pi}{\beta_{r_i}\theta_r}\right)\left[\frac{1}{R_{re}} - \frac{\beta_2}{R_{ri}}\left(\frac{R_{re}}{R_{ri}}\right)^{-k\frac{\pi}{\beta_{r_i}\theta_r}-1}\right] \quad (29)$$

and from (18), the normal derivative of vector-potential in the jth slot at the airgap-stator interface ($r = R_{si}$) is,

$$\left.\frac{\partial A_j(r,\nu)}{\partial r}\right|_{r=R_{si}} = \beta_3 + \sum_{q\geq 1}\left[A_q^{(j)}\Lambda_{1qj} - \Lambda_{2qj}\right] \cos\left(q\frac{\pi}{\beta_{s_j}\theta_s}(\nu-\theta_j)\right) \quad (30)$$

with,

$$\beta_3 = \mu_0\frac{J_{j0}}{2}R_{si}\left(\left(\frac{R_{se}}{R_{si}}\right)^2 - 1\right) \quad (31)$$

$$\Lambda_{1qj} = q\frac{\pi}{\beta_{s_j}\theta_s}\left[-\frac{1}{R_{si}} + \frac{\beta_1}{R_{se}}\left(\frac{R_{si}}{R_{se}}\right)^{q\frac{\pi}{\beta_{s_j}\theta_s}-1}\right] \quad (32)$$

$$\Lambda_{2qj} = 2\mu_o\frac{J_{jq}}{4-\left(q\frac{\pi}{\beta_{s_j}\theta_s}\right)^2}\left(R_{si} - R_{se}\left(\frac{R_{si}}{R_{se}}\right)^{q\frac{\pi}{\beta_{s_j}\theta_s}-1}\right) \quad (33)$$

Now that expressions of the normal derivative of vector-potential in stator or rotor slots are derived (See Eqs. (28) and (30)), functions $\Omega_1(\nu)$ and $\Omega_2(\nu)$ can be extented into Fourier series. Regarding the Fourier series expansion of $\Omega_1(\nu)$,

$$\Omega_1(\nu) = \sum_{n\geq 1}\Upsilon_{1n}\cos(n\nu) + \Gamma_{1n}\sin(n\nu) \quad (34)$$

Fourier series coefficients Υ_{1n} and Γ_{1n} can be determined from (26) and (28) as follows,

$$\begin{aligned}\Upsilon_{1n} &= \frac{1}{\pi}\int_0^{2\pi}\left.\frac{\partial A_i(r,\nu)}{\partial r}\right|_{r=R_{re}}\cos(n\nu)\,d\nu \\ &= \frac{1}{\pi}\sum_{i=1}^{N_r}\int_{\theta_i}^{\theta_i+\beta_{r_i}\theta_r}\left.\frac{\partial A_i(r,\nu)}{\partial r}\right|_{r=R_{re}}\cos(n\nu)\,d\nu \\ &= \frac{1}{\pi}\sum_{i=1}^{N_r}\sum_{k\geq 1}A_k^{(i)}\Lambda_{1k}\alpha_{k,n,i}\end{aligned} \quad (35)$$

and,

$$\begin{aligned}\Gamma_{1n} &= \frac{1}{\pi}\int_0^{2\pi} \left.\frac{\partial A_i(r,\nu)}{\partial r}\right|_{r=R_{re}} \sin(n\nu)\, d\nu \\ &= \frac{1}{\pi}\sum_{i=1}^{N_r} \int_{\theta_i}^{\theta_i+\beta_{r_i}\theta_r} \left.\frac{\partial A_i(r,\nu)}{\partial r}\right|_{r=R_{re}} \sin(n\nu)\, d\nu \\ &= \frac{1}{\pi}\sum_{i=1}^{N_r}\sum_{k\geq 1} A_k^{(i)}\Lambda_{1k}\sigma_{k,n,i} \end{aligned} \tag{36}$$

with $\alpha_{k,n,i}$ and $\sigma_{k,n,i}$ defined respectively by (37) and (38).

As can be seen, in previous integrals (37) and (38), we accounted for the case when $k\pi = n\beta_{r_i}\theta_r$. Another solution lies in the development of those integrals in the form of a product of trigonometric and sine cardinal functions. This development could be meaningful during the numerical implementation, avoiding any conditions on value of denominator.

After calculations, it is possible to write

$$\begin{aligned}\alpha_{k,n,i} = \frac{\beta_{r_i}\theta_r}{2}\Bigg\{&\cos\left(n\left(\theta_i+\frac{\beta_{r_i}\theta_r}{2}\right)-k\frac{\pi}{2}\right) \\ &\operatorname{sinc}\left(\frac{k}{2}-\frac{n\beta_{r_i}}{N_r}\right) \\ &+\cos\left(n\left(\theta_i+\frac{\beta_{r_i}\theta_r}{2}\right)+k\frac{\pi}{2}\right)\operatorname{sinc}\left(\frac{k}{2}+\frac{n\beta_{r_i}}{N_r}\right)\Bigg\}\end{aligned} \tag{39}$$

and

$$\begin{aligned}\sigma_{k,n,i} = \frac{\beta_{r_i}\theta_r}{2}\Bigg\{&\sin\left(n\left(\theta_i+\frac{\beta_{r_i}\theta_r}{2}\right)-k\frac{\pi}{2}\right) \\ &\operatorname{sinc}\left(\frac{k}{2}-\frac{n\beta_{r_i}}{N_r}\right) \\ &+\sin\left(n\left(\theta_i+\frac{\beta_{r_i}\theta_r}{2}\right)+k\frac{\pi}{2}\right)\operatorname{sinc}\left(\frac{k}{2}+\frac{n\beta_{r_i}}{N_r}\right)\Bigg\}\end{aligned} \tag{40}$$

The same procedure is applied to determine Fourier series coefficients Υ_{2n} and Γ_{2n} of function $\Omega_2(\nu)$,

$$\Omega_2(\nu) = \sum_{n\geq 1} \Upsilon_{2n}\cos(n\nu) + \Gamma_{2n}\sin(n\nu) \tag{41}$$

with

$$\begin{aligned}\Upsilon_{2n} &= \frac{1}{\pi}\int_0^{2\pi} \left.\frac{\partial A_j(r,\nu)}{\partial r}\right|_{r=R_{si}} \cos(n\nu)\, d\nu \\ &= \frac{1}{\pi}\sum_{j=1}^{N_s} \int_{\theta_j}^{\theta_j+\beta_{s_j}\theta_s} \left.\frac{\partial A_j(r,\nu)}{\partial r}\right|_{r=R_{si}} \cos(n\nu)\, d\nu \\ &= \frac{1}{\pi}\sum_{j=1}^{N_s}\left\{\beta_3\alpha_{n,j} + \sum_{q\geq 1} A_q^{(i)}\Lambda_{1q}\alpha_{q,n,j} - \Lambda_{2q}\alpha_{q,n,j}\right\}\end{aligned} \tag{42}$$

and

$$\begin{aligned}\Gamma_{2n} &= \frac{1}{\pi}\int_0^{2\pi} \left.\frac{\partial A_j(r,\nu)}{\partial r}\right|_{r=R_{si}} \sin(n\nu)\, d\nu \\ &= \frac{1}{\pi}\sum_{j=1}^{N_s} \int_{\theta_j}^{\theta_j+\beta_{s_j}\theta_s} \left.\frac{\partial A_j(r,\nu)}{\partial r}\right|_{r=R_{si}} \sin(n\nu)\, d\nu \\ &= \frac{1}{\pi}\sum_{j=1}^{N_s}\left\{\beta_3\sigma_{n,j} + \sum_{q\geq 1} A_q^{(i)}\Lambda_{1q}\sigma_{q,n,j} - \Lambda_{2q}\sigma_{q,n,j}\right\}\end{aligned} \tag{43}$$

Integrals $\alpha_{q,n,j}$ and $\sigma_{q,n,j}$ can be derived as follows,

$$\begin{aligned}\alpha_{q,n,j} = \frac{\beta_{s_j}\theta_s}{2}\Bigg\{&\cos\left(n\left(\theta_j+\frac{\beta_{s_j}\theta_s}{2}\right)-q\frac{\pi}{2}\right) \\ &\operatorname{sinc}\left(\frac{q}{2}-\frac{n\beta_{s_j}}{N_s}\right) \\ &+\cos\left(n\left(\theta_j+\frac{\beta_{s_j}\theta_s}{2}\right)+q\frac{\pi}{2}\right)\operatorname{sinc}\left(\frac{q}{2}+\frac{n\beta_{s_j}}{N_s}\right)\Bigg\}\end{aligned} \tag{44}$$

and

$$\begin{aligned}\sigma_{q,n,j} = \frac{\beta_{s_j}\theta_s}{2}\Bigg\{&\sin\left(n\left(\theta_j+\frac{\beta_{s_j}\theta_s}{2}\right)-q\frac{\pi}{2}\right) \\ &\operatorname{sinc}\left(\frac{q}{2}-\frac{n\beta_{s_j}}{N_s}\right) \\ &+\sin\left(n\left(\theta_j+\frac{\beta_{s_j}\theta_s}{2}\right)+q\frac{\pi}{2}\right)\operatorname{sinc}\left(\frac{q}{2}+\frac{n\beta_{s_j}}{N_s}\right)\Bigg\}\end{aligned} \tag{45}$$

The normal derivative of vector-potential in the airgap region can be expressed at its internal radius ($r = R_{re}$) as follows,

$$\begin{aligned}\left.\frac{\partial A_I(r,\nu)}{\partial r}\right|_{r=R_{re}} = &\sum_{n\geq 1} n\left[-\frac{A_n^{(I)}}{R_{re}} + \frac{B_n^{(I)}}{R_{si}}\left(\frac{R_{re}}{R_{si}}\right)^{n-1}\right] \\ &\cos(n\nu) \\ &+ n\left[-\frac{C_n^{(I)}}{R_{re}} + \frac{D_n^{(I)}}{R_{si}}\left(\frac{R_{re}}{R_{si}}\right)^{n-1}\right]\sin(n\nu)\end{aligned} \tag{46}$$

ans at its external radius ($r = R_{si}$),

$$\begin{aligned}\left.\frac{\partial A_I(r,\nu)}{\partial r}\right|_{r=R_{si}} = &\sum_{n\geq 1} n\left[-\frac{A_n^{(I)}}{R_{re}}\left(\frac{R_{si}}{R_{re}}\right)^{-n-1} + \frac{B_n^{(I)}}{R_{si}}\right] \\ &\cos(n\nu) \\ &+ n\left[-\frac{C_n^{(I)}}{R_{re}}\left(\frac{R_{si}}{R_{re}}\right)^{-n-1} + \frac{D_n^{(I)}}{R_{si}}\right]\sin(n\nu)\end{aligned} \tag{47}$$

According to boundary conditions (26) and (27), and from (34), (41), (46) and (47), we can set up the following equations,

$$\frac{1}{\pi}\sum_{i=1}^{N_r}\sum_{k\geq 1}A_k^{(i)}\Lambda_{1k}\alpha_{k,n,i} = n\left[-\frac{A_n^{(I)}}{R_{re}}+\frac{B_n^{(I)}}{R_{si}}\left(\frac{R_{re}}{R_{si}}\right)^{n-1}\right] \tag{48}$$

$$\frac{1}{\pi}\sum_{j=1}^{N_s}\left\{\beta_3\alpha_{n,j}+\sum_{q\geq 1}A_q^{(i)}\Lambda_{1q}\alpha_{q,n,j}-\Lambda_{2q}\alpha_{q,n,j}\right\} = n\left[-\frac{A_n^{(I)}}{R_{re}}\left(\frac{R_{si}}{R_{re}}\right)^{-n-1}+\frac{B_n^{(I)}}{R_{si}}\right] \tag{49}$$

$$\frac{1}{\pi}\sum_{i=1}^{N_r}\sum_{k\geq 1}A_k^{(i)}\Lambda_{1k}\sigma_{k,n,i} = n\left[-\frac{C_n^{(I)}}{R_{re}}+\frac{D_n^{(I)}}{R_{si}}\left(\frac{R_{re}}{R_{si}}\right)^{n-1}\right] \tag{50}$$

$$\frac{1}{\pi}\sum_{j=1}^{N_s}\left\{\beta_3\sigma_{n,j}+\sum_{q\geq 1}A_q^{(i)}\Lambda_{1q}\sigma_{q,n,j}-\Lambda_{2q}\sigma_{q,n,j}\right\} = n\left[-\frac{C_n^{(I)}}{R_{re}}\left(\frac{R_{si}}{R_{re}}\right)^{-n-1}+\frac{D_n^{(I)}}{R_{si}}\right] \tag{51}$$

2) Continuity of Vector-potential

The second condition that has to be ensured is the continuity of vector-potential between two domains (Fig. 7). For the internal radius of the airgap ($r = R_{re}$), it means that the vector-potential of the airgap over each rotor slot equals the vector-potential of the rotor slots,

$$A_i(r,\nu)|_{r=R_{re}} = A_I(r,\nu)|_{r=R_{re}} \text{ for } \nu\in[\theta_i,\theta_i+\beta_{r_i}\theta_r] \tag{52}$$

Similarly, at the airgap external radius ($r = R_{si}$), the vector-potential of the airgap over each stator slot has to equal the vector-potential of the corresponding stator slot,

$$A_j(r,\nu)|_{r=R_{si}} = A_I(r,\nu)|_{r=R_{si}} \text{ for } \nu\in[\theta_j,\theta_j+\beta_{s_j}\theta_s] \tag{53}$$

However, expressions of vector-potential in each region do not have the same spacial frequency. This means that vector-potential of airgap over each stator and rotor slots has to be extended into Fourier series to satisfy the vector-potential continuity condition.

Herefater, we first consider condition (52). The airgap vector-potential expression (5) is expended into Fourier series

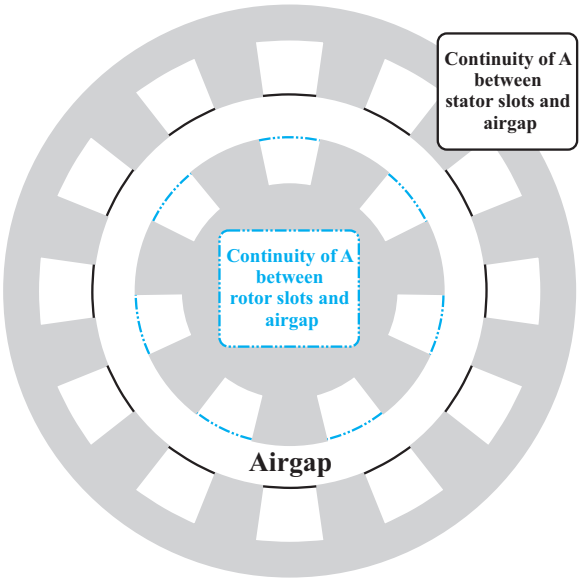

Fig. 7. Shematic representation of airgap domain surrounded by stator and rotor cores - Continuity of vector-potential between airgap domain and respectively the rotor (blue dotted lines) and the stator (black solid lines)

over the ith rotor slot opening at $r = R_{re}$. It gives for the mean value,

$$\begin{aligned}A_0^{(i)} &= \frac{1}{\beta_{r_i}\theta_r}\int_{\theta_i}^{\theta_i+\beta_{r_i}\theta_r}A_I(r=R_{re},\nu)\,d\nu \\ &= \frac{1}{\beta_{r_i}\theta_r}\sum_{n\geq 1}\left\{\left[A_n^{(I)}+B_n^{(I)}\left(\frac{R_{re}}{R_{si}}\right)^n\right]\alpha_{n,i} + \left[C_n^{(I)}+D_n^{(I)}\left(\frac{R_{re}}{R_{si}}\right)^n\right]\sigma_{n,i}\right\}\end{aligned} \tag{54}$$

with

$$\begin{aligned}\alpha_{n,i} &= \int_{\theta_i}^{\theta_i+\beta_{r_i}\theta_r}\cos(n\nu)\,d\nu \\ &= \frac{\sin(n(\theta_i+\beta_{r_i}\theta_r))-\sin(n\theta_i)}{n}\end{aligned} \tag{55}$$

and

$$\alpha_{k,n,i} = \int_{\theta_i}^{\theta_i+\beta_{r_i}\theta_r}\cos\left(k\frac{\pi}{\beta_{r_i}\theta_r}(\nu-\theta_i)\right)\cos(n\nu)\,d\nu = \begin{cases}\frac{n\left(\beta_{r_i}\theta_r\right)^2\left(\sin(n\theta_i)-\sin\left(n\left(\theta_i+\beta_{r_i}\theta_r\right)\right)(-1)^k\right)}{(k\pi)^2-\left(n\beta_{r_i}\theta_r\right)^2} & \text{for } k\pi\neq n\beta_{r_i}\theta_r \\ \frac{\beta_{r_i}\theta_r\cos(n\theta_i)}{2}-\frac{\sin(n\theta_i)-\sin\left(n\theta_i+2n\beta_{r_i}\theta_r\right)}{4n} & \text{for } k\pi = n\beta_{r_i}\theta_r\end{cases} \tag{37}$$

$$\sigma_{k,n,i} = \int_{\theta_i}^{\theta_i+\beta_{r_i}\theta_r}\cos\left(k\frac{\pi}{\beta_{r_i}\theta_r}(\nu-\theta_i)\right)\sin(n\nu)\,d\nu = \begin{cases}\frac{-n\left(\beta_{r_i}\theta_r\right)^2\left(\cos(n\theta_i)-\cos\left(n\left(\theta_i+\beta_{r_i}\theta_r\right)\right)(-1)^k\right)}{(k\pi)^2-\left(n\beta_{r_i}\theta_r\right)^2} & \text{for } k\pi\neq n\beta_{r_i}\theta_r \\ \frac{\beta_{r_i}\theta_r\sin(n\theta_i)}{2}+\frac{\cos(n\theta_i)-\cos\left(n\theta_i+2n\beta_{r_i}\theta_r\right)}{4n} & \text{for } k\pi = n\beta_{r_i}\theta_r\end{cases} \tag{38}$$

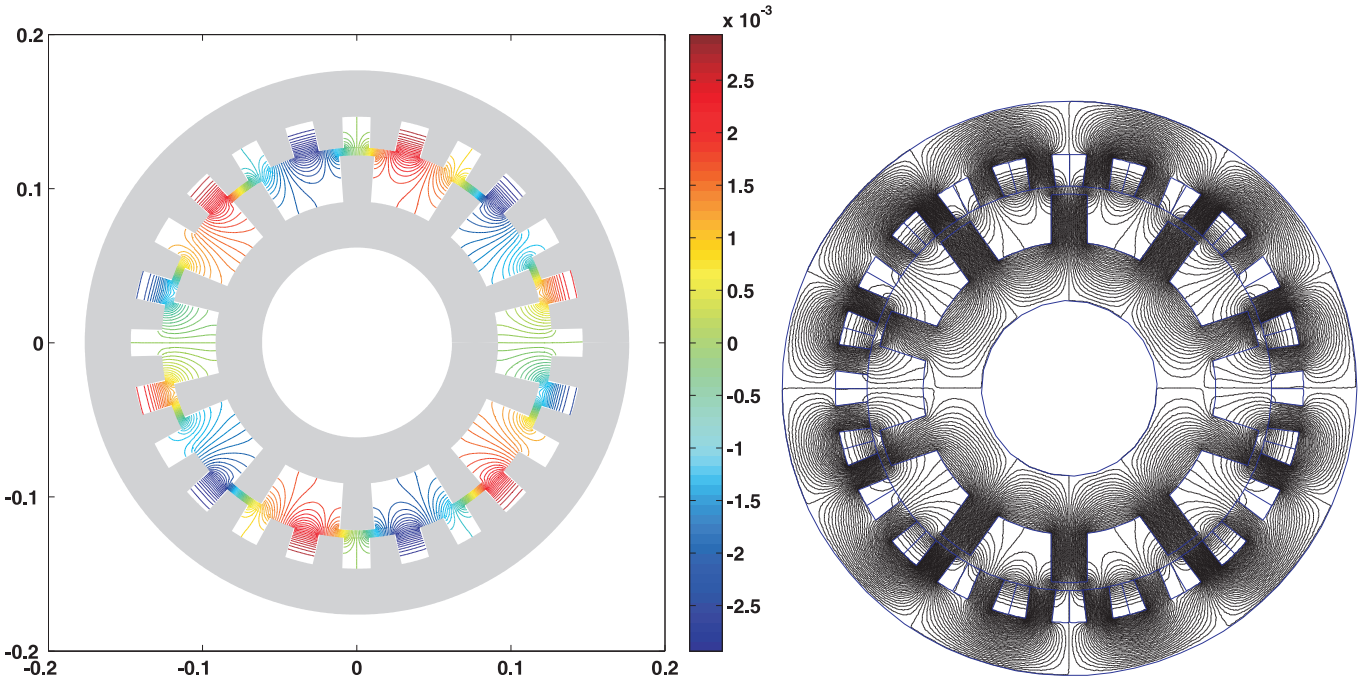

(a) (b)

Fig. 8. Distribution of equipotential lines of magnetic vector-potential in air-gap and rotor/stator slot regions with the analytical model (a) and 2D FE simulation (b). Classical 24-10 FE-SF topology at no-load - $NI_{exc} = 1200A.tr$ - $\beta_s = 0.5$ - $\beta_r = 0.7$ - $N = 150$ - $K = Q = 20$

$$\sigma_{n,i} = \int_{\theta_i}^{\theta_i+\beta_{r_i}\theta_r} \sin(n\nu)\, d\nu = \frac{\cos(n\theta_i) - \cos(n(\theta_i + \beta_{r_i}\theta_r))}{n} \tag{56}$$

and for the kth harmonic, we can write that

$$\begin{aligned} & A_k^{(i)} \left[\beta_2 \left(\frac{R_{re}}{R_{ri}} \right)^{-k\frac{\pi}{\beta_{r_i}\theta_r}} + 1 \right] \\ &= \frac{2}{\beta_{r_i}\theta_r} \int_{\theta_i}^{\theta_i+\beta_{r_i}\theta_r} A_I(r = R_{re}, \nu) \cos\left(k \frac{\pi}{\beta_{r_i}\theta_r} (\nu - \theta_i) \right) d\nu \\ &= \frac{2}{\beta_{r_i}\theta_r} \sum_{n\geq 1} \left\{ \left[A_n^{(I)} + B_n^{(I)} \left(\frac{R_{re}}{R_{si}} \right)^n \right] \alpha_{k,n,i} \right. \\ &\quad \left. + \left[C_n^{(I)} + D_n^{(I)} \left(\frac{R_{re}}{R_{si}} \right)^n \right] \sigma_{k,n,i} \right\} \end{aligned} \tag{57}$$

From (18) and (5), it is possible to derive the Fourier series expression of the airgap vector-potential over the jth stator slot opoening at $r = R_{si}$,

$$\begin{aligned} & A_0^{(j)} + \mu_0 \frac{J_{j0}}{2} \left(R_{se}^2 \ln(R_{si}) - \frac{R_{si}^2}{2} \right) \\ &= \frac{1}{\beta_{s_j}\theta_s} \int_{\theta_j}^{\theta_j+\beta_{s_j}\theta_s} A_I(r = R_{si}, \nu)\, d\nu \\ &= \frac{1}{\beta_{s_j}\theta_s} \sum_{n\geq 1} \left\{ \left[A_n^{(I)} \left(\frac{R_{si}}{R_{re}} \right)^{-n} + B_n^{(I)} \right] \alpha_{n,j} \right. \\ &\quad \left. + \left[C_n^{(I)} \left(\frac{R_{si}}{R_{re}} \right)^{-n} + D_n^{(I)} \right] \sigma_{n,j} \right\} \end{aligned} \tag{58}$$

with

$$\alpha_{n,j} = \int_{\theta_j}^{\theta_j+\beta_{s_j}\theta_s} \cos(n\nu)\, d\nu = \frac{\sin\left(n\left(\theta_j + \beta_{s_j}\theta_s\right)\right) - \sin(n\theta_j)}{n} \tag{59}$$

and

$$\sigma_{n,j} = \int_{\theta_j}^{\theta_j+\beta_{s_j}\theta_s} \sin(n\nu)\, d\nu = \frac{\cos(n\theta_j) - \cos\left(n\left(\theta_j + \beta_{s_j}\theta_s\right)\right)}{n} \tag{60}$$

for the mean value, and

$$\begin{aligned} & \left[A_q^{(j)} \left[1 + \beta_1 \left(\frac{R_{si}}{R_{se}} \right)^{q\frac{\pi}{\beta_{s_j}\theta_s}} \right] \right. \\ & \left. -\mu_o \frac{J_{jq}}{4 - \left(q\frac{\pi}{\beta_{s_j}\theta_s} \right)^2} \left(R_{si}^2 - \frac{2R_{se}^2}{\left(q\frac{\pi}{\beta_{s_j}\theta_s} \right)} \left(\frac{R_{si}}{R_{se}} \right)^{q\frac{\pi}{\beta_{s_j}\theta_s}} \right) \right] \end{aligned}$$

$$= \frac{2}{\beta_{s_j}\theta_s} \int_{\theta_j}^{\theta_j+\beta_{s_j}\theta_s} A_I\left(r=R_{si},\nu\right)\cos\left(q\frac{\pi}{\beta_{s_j}\theta_s}\left(\nu-\theta_j\right)\right)d\nu$$

$$= \frac{2}{\beta_{s_j}\theta_s}\left\{\sum_{n\geq 1}\left[A_n^{(I)}\left(\frac{R_{si}}{R_{re}}\right)^{-n}+B_n^{(I)}\right]\alpha_{q,n,j} + \left[C_n^{(I)}\left(\frac{R_{si}}{R_{re}}\right)^{-n}+D_n^{(I)}\right]\sigma_{q,n,j}\right\} \quad (61)$$

for the qth harmonic term.

Finally, equations (48), (49), (50), (51), (54), (57), (58) and (61) can be rewritten into matrix and vector form to get a numerical solution of the unknown coefficients A_n, B_n, C_n, D_n, $A_0^{(i)}$, $A_k^{(i)}$, $A_0^{(j)}$ and $A_q^{(j)}$. It should be noted that mean values of vector-potential in rotor slots $A_0^{(i)}$ and stator slots $A_0^{(j)}$ are not primarily needed to solve the linear system. They could be evaluated afterwards using airgap harmonic coefficients obtained numerically.

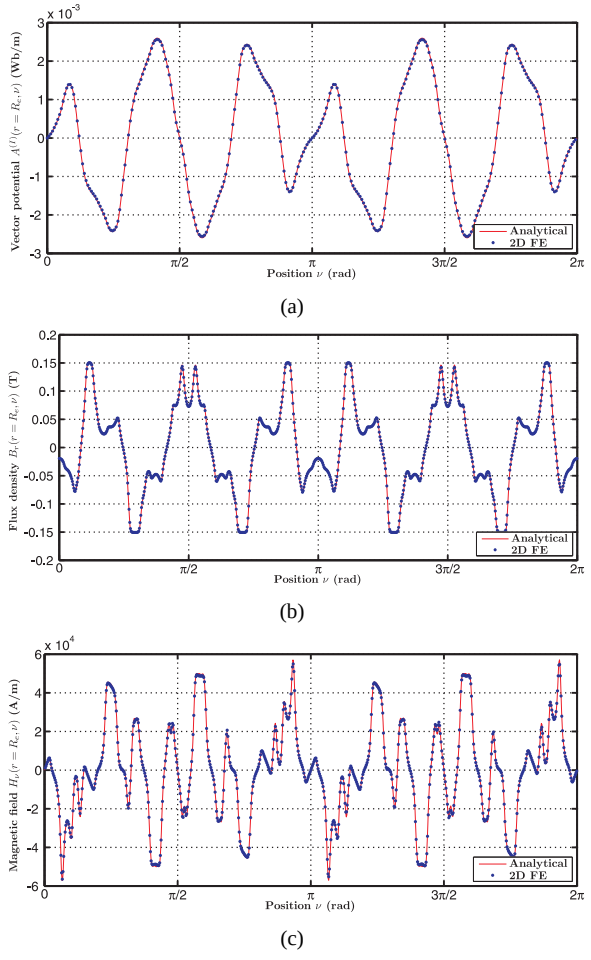

(a) (b) (c)

Fig. 9. Evaluation of vector-potential $A^{(I)}(r=R_e,\nu)$ (a), radial flux density $B_r(r=R_e,\nu)$ (b) and tangential magnetic field $H_\nu(r=R_e,\nu)$ (c) along the mean airgap with the analytical model and 2D FE simulation for a classical 24-10 FE-SF topology at no-load - $NI_{exc}=1200A.tr$ - $\beta_s=0.5$ - $\beta_r=0.7$ - $N=150$ - $K=Q=20$

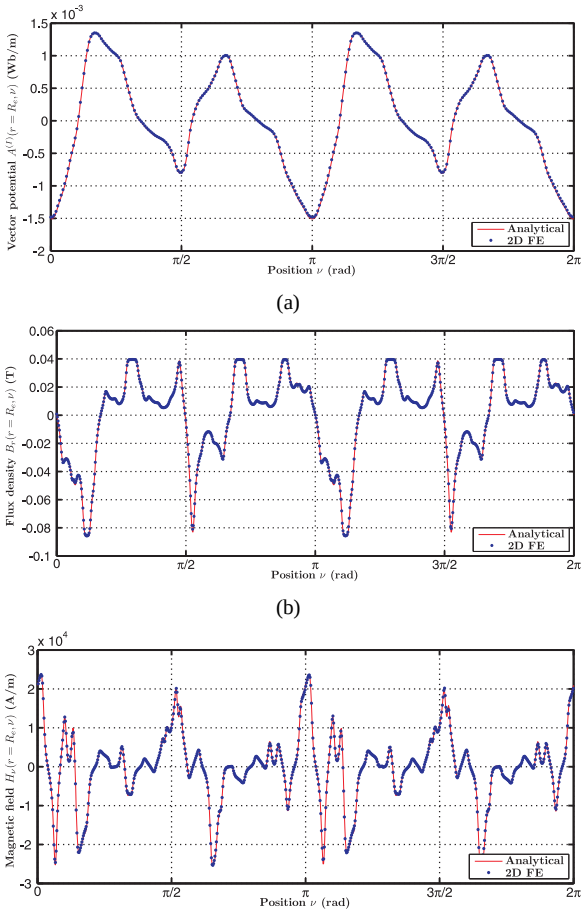

(a) (b) (c)

Fig. 10. Evaluation of vector-potential $A^{(I)}(r=R_e,\nu)$ (a), radial flux density $B_r(r=R_e,\nu)$ (b) and tangential magnetic field $H_\nu(r=R_e,\nu)$ (c) along the mean airgap with the analytical model and 2D FE simulation for a classical 24-10 FE-SF topology with double layer configuration - Only phase a is powered with $NI_a=500A.tr$ - $\beta_s=0.5$ - $\beta_r=0.7$ - $N=150$ - $K=Q=20$

IV. Airgap Field Calculations and Finite Elements Comparisons

The foregoing analytical model for conventional and alternate Field-Excited Swithed-Flux topologies is used to determine both no-load, armature reaction and on-load magnetic field distribution at the mean airgap radius. The main machines dimensions are reminded in Table I. Analytical airgap field predictions are extensively compared to 2D FE calcultations. As for the analytical model, a highly permeable linear material ($\mu_r=5000$) is considered in the 2D FE simulations. Also, in 2D FE simulations, we considered structures having straight teeth.

The vector-potential in the middle of the airgap can be directly evaluated from (5) as follows,

The radial component of flux density and tangential component of magnetic field at the mean radius of airgap domain can be derived from $\overrightarrow{B}=rot\left(\overrightarrow{A}\right)$,

$$\begin{cases} B_r^{(I)}\left(r,\nu\right)=\frac{1}{r}\frac{\partial A^{(I)}(r,\nu)}{\partial \nu} \\ H_\nu^{(I)}\left(r,\nu\right)=-\frac{1}{\mu_0}\frac{\partial A^{(I)}(r,\nu)}{\partial r} \end{cases} \quad (62)$$

Description	Symbol	Numerical value
Common parameters		
Outer radius of stator	R_{se}	$146.6mm$
Inner radius of stator	R_{si}	$126.6mm$
Mean airgap radius	R_e	$124.1mm$
Outer radius of rotor	R_{re}	$121.6mm$
Inner radius of rotor	R_{ri}	$91.6mm$
Active length	L_a	$45mm$
DC winding MMF	NI_{exc}	$1000A.tr$
Peak phase MMF	NI_{phase}	$500A.tr$
Number of phase	q	3
Classical FE-SF machine		
Number of stator tooth	N_s	24
Number of rotor tooth	N_r	10
Alternate FE-SF machine with spacer tooth		
Number of stator teeth	N_s	18
Number of rotor teeth	N_r	11

TABLE I
MAIN PARAMETERS OF CLASSICAL AND ALTERNATE FE-SF TOPOLOGIES

Finally, it yields to

$$B_r^{(I)}(R_e,\nu) = \sum_{n\geq 1} n\left[\frac{C_n^{(I)}}{R_e}\left(\frac{R_e}{R_{re}}\right)^{-n} + \frac{D_n^{(I)}}{R_e}\left(\frac{R_e}{R_{si}}\right)^{n}\right] \cos(n\nu) - n\left[\frac{A_n^{(I)}}{R_e}\left(\frac{R_e}{R_{re}}\right)^{-n} + \frac{B_n^{(I)}}{R_e}\left(\frac{R_e}{R_{si}}\right)^{n}\right]\sin(n\nu) \quad (63)$$

for the radial component of flux density $B_r^{(I)}(R_e,\nu)$, and

$$H_\nu^{(I)}(R_e,\nu) = \frac{1}{\mu_0}\sum_{n\geq 1} n\left[\frac{A_n^{(I)}}{R_{re}}\left(\frac{R_e}{R_{re}}\right)^{-n-1} - \frac{B_n^{(I)}}{R_{si}}\left(\frac{R_e}{R_{si}}\right)^{n-1}\right]\cos(n\nu) + n\left[\frac{C_n^{(I)}}{R_{re}}\left(\frac{R_e}{R_{re}}\right)^{-n-1} - \frac{D_n^{(I)}}{R_{si}}\left(\frac{R_e}{R_{si}}\right)^{n-1}\right]\sin(n\nu) \quad (64)$$

for the tangential component of magnetic field $H_\nu^{(I)}(R_e,\nu)$.

A. Classical FE-SF machine

We first investigate classical FE-SF machine with 24 stator slots, 10 rotor teeth and a double-layer winding configuration. The vector-potential in the whole airgap, including rotor and stator slots is analytically calculated according to (5), (24) and (18) and equipotential lines of vector-potential are depicted in Fig. 8.

As can be seen, boundary conditions between each region are respected. In Fig. 8.b, equipotential lines of A obtained with a 2D Finite Element Software are proposed, including the ferromagnetic parts. Regarding the distribution of A in the airgap domain, it is shown that the analytical model gives us an excellent evaluation of A. We compared in Figs. 9, 10 and 11, distributions of vector-potential A, radial flux density B_r and circumferential magnetic field H_ν in the airgap ($r = R_e$) at no-load (only DC excitation windings powered), armature reaction and on-load conditions respectively. Analytical predictions are in close agreement with those computed by 2D FE.

In addition, the airgap field, either radial or circumferential, presents a high harmonic content. Nevertheless, the analytical model still exhibits high accuracy. This gives meaning to the use of Fourier harmonic modeling technique for the analysis of FE-SF machines.

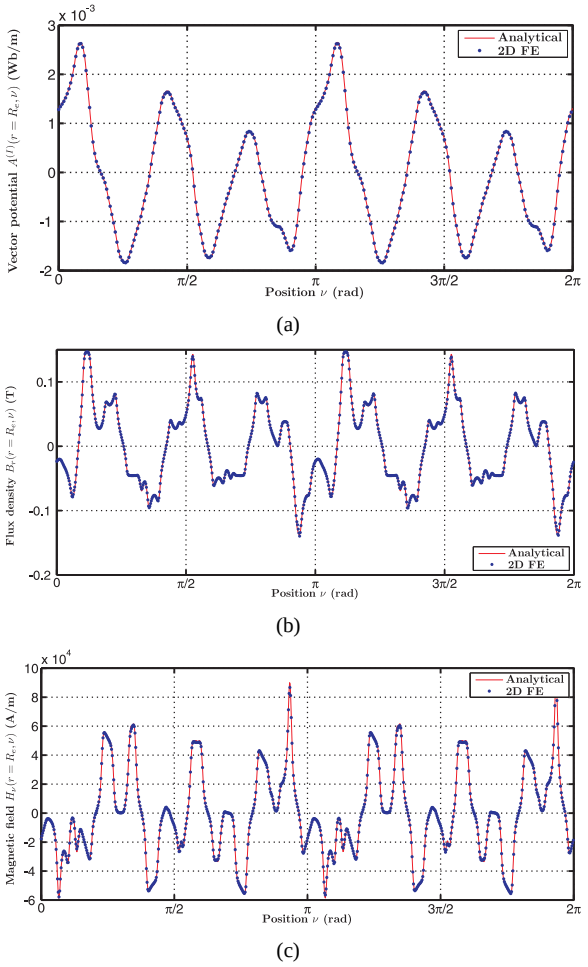

Fig. 11. Evaluation of vector-potential $A^{(I)}(r = R_e,\nu)$ (a), radial flux density $B_r(r = R_e,\nu)$ (b) and tangential magnetic field $H_\nu(r = R_e,\nu)$ (c) along the mean airgap with the analytical model and 2D FE simulation for a classical 24-10 FE-SF topology with double layer configuration - On-load with sinusoidal feeding currents - $NI_{phase} = 500A.tr$ - $\beta_s = 0.5$ - $\beta_r = 0.7$ - $N = 150$ - $K = Q = 20$

B. Unconventional FE-SF machine with spacer teeth

It is of paramount interest of that the foregoing analytical solution of magnetic field allows exploration of unconventional Field-Excited Switched-Flux machines. Indeed, those structures usually require modifications of phase coil connections. To do so, we used a connecting matrix C (size $4 \times 2N_s$) defining coils distributions in the stator slots. For illustrative purpose, the connecting coil matrix of the 24-10 FE-SF machine with double-layer windings is given by (65). Regarding the unconventional 18-11 FE-SF machine with spacer teeth and single-layer winding, the matrix C can be defined as (66).

In Fig. 12, the equipotential line distribution of vector-potential A at no-load for the 18-11 FE-SF, analytically-predicted or FE-calculated, are proposed. Obviously, the analytical model can fairly predict A in the whole airgap domain. We compare once again distributions of vector-potential A, radial flux density B_r and circumferential magnetic field H_ν in the airgap ($r = R_e$) obtained with FE simulations and with the model for different load conditions (See Figs. 13, 14 and 15). Each comparison exhibits good agreement. Also, it should be noted that the airgap field distribution are 2π-periodic because of the odd number of teeth.

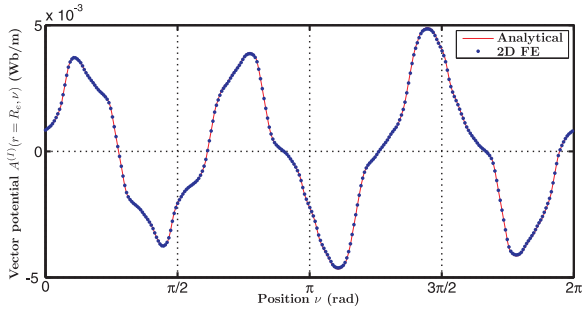

(a)

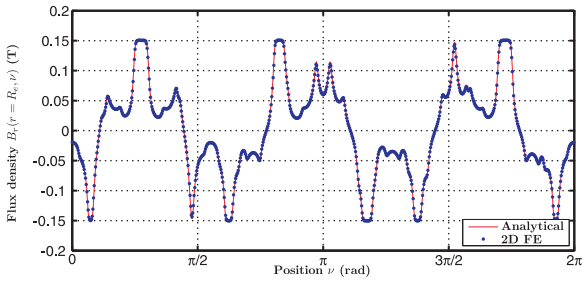

(b)

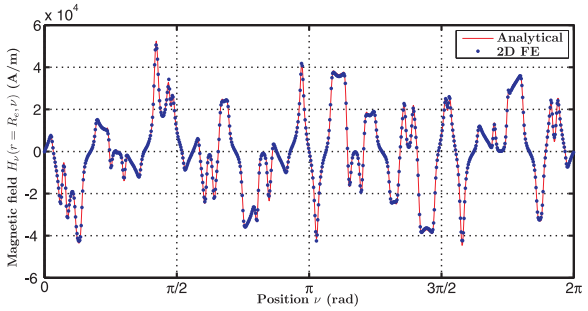

(c)

Fig. 13. Evaluation of vector-potential $A^{(I)}(r = R_e, \nu)$ (a), radial flux density $B_r(r = R_e, \nu)$ (b) and tangential magnetic field $H_\nu(r = R_e, \nu)$ (c) along the mean airgap with the analytical model and 2D FE simulation for an unconventional 18-11 FE-SF topology with spacer teeth at no-load - $NI_{exc} = 1200A.tr$ - $\beta_s = 0.5$ - $\beta_r = 0.7$ - $N = 150$ - $K = Q = 20$

V. Conclusion

An improved analytical model to describe the magnetic field in the doubly-slotted airgap of Field-Excited Flux-Switching is proposed in this paper. The whole airgap domain is divided in three types of regions, i.e. stator slots, airgap and rotor slots. General expressions of vector-potential are derived for each subdomain by the variable separation method, and the field

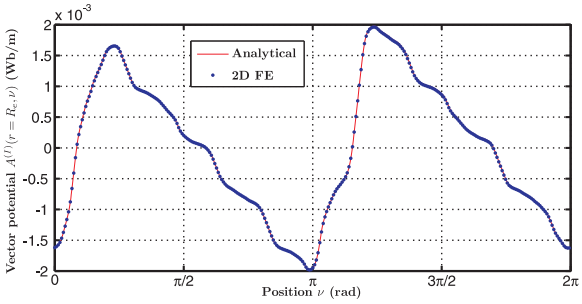

(a)

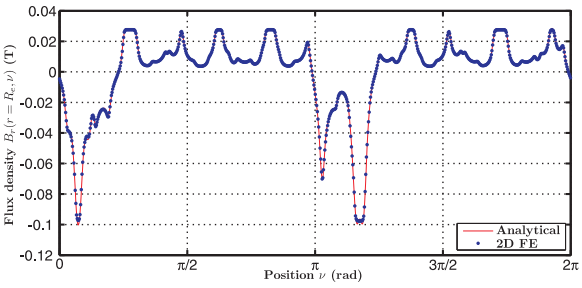

(b)

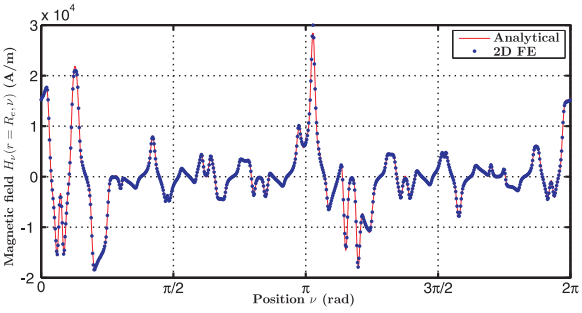

(c)

Fig. 14. Evaluation of vector-potential $A^{(I)}(r = R_e, \nu)$ (a), radial flux density $B_r(r = R_e, \nu)$ (b) and tangential magnetic field $H_\nu(r = R_e, \nu)$ (c) along the mean airgap with the analytical model and 2D FE simulation for an unconventional 18-11 FE-SF topology with spacer teeth - Only phase a is powered with $NI_a = 500A.tr$ - $\beta_s = 0.5$ - $\beta_r = 0.7$ - $N = 150$ - $K = Q = 20$

solution is then obtained by applying the boundary integral method.

In addition, the model is derived in a general manner so that it can be extended rapidly to unconventional FE-SF structures. Indeed, it allows a fast exploration of unconventional structures with different winding configuration or stator-rotor teeth combination. By means of example, an unconventional FE-SF machine with spacer teeth is presented.

Analytical predictions of airgap field for both conventional and alternate FE-SF topologies are extensively compared to 2D FE simulations. Comparisons show good agreement for numerous load-conditions. This result highlights the merits of harmonic modeling technique for the analysis of FE-SF machines.

Finally, from radial magnetic flux-density and circumferential magnetic field predictions, instantaneous electromagnetic torque can be assessed according to the Maxwell stress tensor (See Appendix B). Comparative study of optimized electromagnetic performances of FE-SF machines will be presented

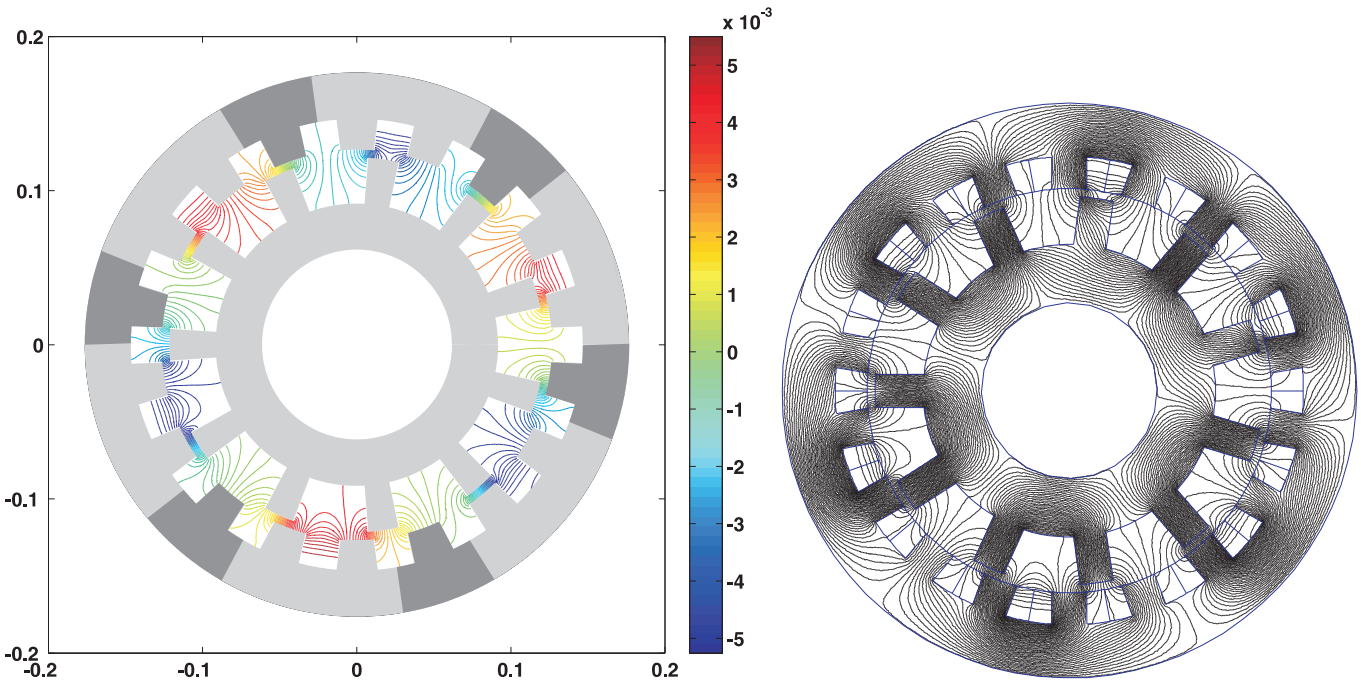

Fig. 12. Distribution of equipotential lines of magnetic vector-potential in air-gap and rotor/stator slot regions with the analytical model (a) and 2D FE simulation (b). Unconventional 18-11 FE-SF topology with spacer teeth at no-load - $NI_{exc} = 1200A.tr$ - $\beta_s = 0.5$ - $\beta_r = 0.7$ - $N = 150$ - $K = Q = 20$

in a subsequent paper.

APPENDIX A
CONNECTING COIL MATRIX C FOR CLASSICAL AND UNCONVENTIONAL FE-SF MACHINES

The connecting coil matrix of the 24-10 FE-SF machine with double-layer windings is defined in (65), and for the 18-11 FE-SF machine with spacer teeth and single-layer winding by (66).

APPENDIX B
ELECTROMAGNETIC TORQUE CALCULATION

As explained before, the electromagnetic torque can be calculated analytically according to the Maxwell stress tensor. Fig. 16 presents a comparison between the electromagnetic torque calculated with the analytical model and with 2D FE simulation. As can be seen, both are in good agreement.

ACKNOWLEDGMENT

The authors would like to thank Leroy Somer (which are part of Emerson) and Agence Nationale de la Recherche (ANR) for their support.

REFERENCES

[1] S. E. Rauch and L. J. Johnson, "Design principles of flux-switch alternators," *Power Apparatus and Systems, Part III. Transactions of the American Institute of Electrical Engineers*, vol. 74, no. 3, pp. 1261 –1268, jan. 1955.

[2] E. Hoang, A. H. Ben-Ahmed, and J. Lucidarme, "Switching flux permanent magnet polyphased synchronous machines," in *7th European Conference on Power Electronics and Applications*, vol. 3, 1997, pp. 903–908.

[3] B. Sarlioglu, Y. Zhao, and T. Lipo, "A novel doubly salient single phase permanent magnet generator," in *Industry Applications Society Annual Meeting, 1994., Conference Record of the 1994 IEEE*, oct 1994, pp. 9 –15 vol.1.

[4] Z. Zhu and J. Chen, "Advanced flux-switching permanent magnet brushless machines," *Magnetics, IEEE Transactions on*, vol. 46, no. 6, pp. 1447 –1453, june 2010.

[5] Z. Zhu, A. Thomas, J. Chen, and G. Jewell, "Cogging torque in flux-switching permanent magnet machines," *IEEE Trans. Magn.*, vol. 45, no. 10, pp. 4708 –4711, oct. 2009.

[6] Y. Cheng, C. Pollock, and H. Pollock, "A permanent magnet flux switching motor for low energy axial fans," in *Industry Applications Conference, 2005. Fourtieth IAS Annual Meeting. Conference Record of the 2005*, vol. 3, oct. 2005, pp. 2168 – 2175 Vol. 3.

[7] C.-F. Wang, J.-X. Shen, Y. Wang, L.-L. Wang, and M.-J. Jin, "A new method for reduction of detent force in permanent magnet flux-switching linear motors," *IEEE Trans. Magn.*, vol. 45, no. 6, pp. 2843 –2846, june 2009.

[8] G. Zhang, M. Cheng, W. Hua, and J. Dong, "Analysis of the oversaturated effect in hybrid excited flux-switching machines," *IEEE Trans. Magn.*, vol. 47, no. 10, pp. 2827 –2830, oct. 2011.

[9] Y. Wang and Z. Deng, "Comparison of hybrid excitation topologies for flux-switching machines," *IEEE Trans. Magn.*, vol. 48, no. 9, pp. 2518 –2527, sept. 2012.

[10] E. Hoang, M. Lecrivain, S. Hlioui, and M. Gabsi, "Hybrid excitation synchronous permanent magnets synchronous machines optimally designed for hybrid and full electrical vehicle," in *Power Electronics and ECCE Asia (ICPE ECCE), 2011 IEEE 8th International Conference on*, 30 2011-june 3 2011, pp. 153 –160.

[11] E. Hoang, M. Gabsi, M. Lecrivain, and B. Multon, "Influence of magnetic losses on maximum power limits of synchronous permanent magnet drives in flux-weakening mode," in *Industry Applications Conference, 2000. Conference Record of the 2000 IEEE*, vol. 1, 2000, pp. 299 –303 vol.1.

[12] Y. Amara, E. Hoang, M. Gabsi, M. Lcrivain, and S. Allano, "Design and comparison of different flux-switch synchronous machines for an aircraft oil breather application," *European Transactions on Electrical Power*, vol. 15, pp. 497–511, 2005.

[13] E. Sulaiman, T. Kosaka, and N. Matsui, "High power density design of 6-slot 8-pole hybrid excitation flux switching machine for hybrid electric vehicles," *IEEE Trans. Magn.*, vol. 47, no. 10, pp. 4453 –4456, oct. 2011.

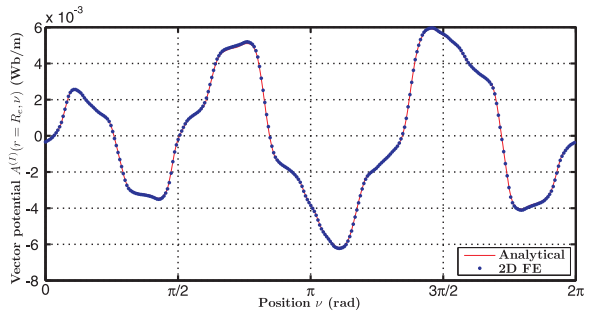

(a)

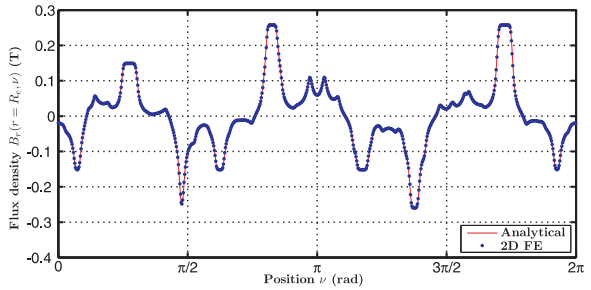

(b)

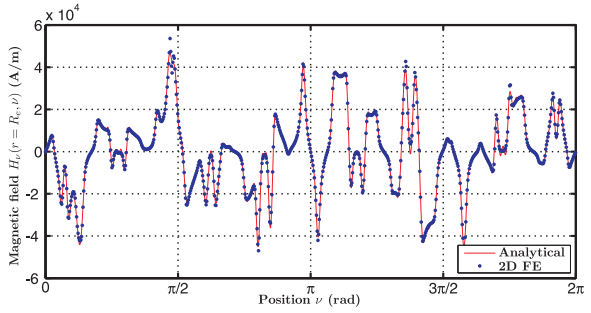

(c)

Fig. 15. Evaluation of vector-potential $A^{(I)}(r = R_e, \nu)$ (a), radial flux density $B_r(r = R_e, \nu)$ (b) and tangential magnetic field $H_\nu(r = R_e, \nu)$ (c) along the mean airgap with the analytical model and 2D FE simulation for an unconventional 18-11 FE-SF topology with spacer teeth - On-load with sinusoidal feeding currents - $NI_{phase} = 500A.tr$ - $\beta_s = 0.5$ - $\beta_r = 0.7$ - $N = 150$ - $K = Q = 20$

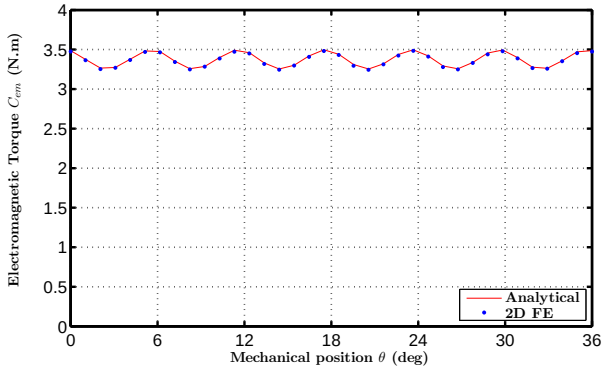

Fig. 16. Evolution of the electromagnetic torque as function of rotor position using the Maxwell stress tensor with the analytical model and 2D FE simulation for a classical 24-10 FE-SF topology with double layer configuration - On-load with sinusoidal feeding currents - $NI_{exc} = 1000A.tr$ - $NI_{phase} = 1000A.tr$ - $\beta_s = 0.5$ - $\beta_r = 0.75$

[14] R. Owen, Z. Zhu, and G. Jewell, "Hybrid-excited flux-switching permanent-magnet machines with iron flux bridges," *IEEE Trans. Magn.*, vol. 46, no. 6, pp. 1726 –1729, june 2010.

[15] W. Hua, M. Cheng, and G. Zhang, "A novel hybrid excitation flux-switching motor for hybrid vehicles," *IEEE Trans. Magn.*, vol. 45, no. 10, pp. 4728 –4731, oct. 2009.

[16] E. Hoang, M. Lecrivain, and M. Gabsi, "A new structure of a switching flux synchronous polyphased machine with hybrid excitation," in *Power Electronics and Applications, 2007 European Conference on*, sept. 2007, pp. 1 –8.

[17] B. Gaussens, E. HOANG, O. de la Barriere, J. Saint-Michel, P. MANFE, M. LECRIVAIN, and M. Gabsi, "A new hybrid-excited flux-switching machine with excitation coils in stator slots," in *Electrical Machines and Systems, 2012. ICEMS 2012. Proceedings of the 15th International Conference on*, 2012.

[18] R. Owen, Z. Zhu, J. Wang, D. A. Stone, and I. Urquhart, "Review of variable-flux permanent magnet machines," in *International Conference on Electrical Machines and Systems, Beijing, China*, 2011.

[19] J. Chen, Z. Zhu, S. Iwasaki, and R. Deodhar, "Low cost flux-switching brushless ac machines," in *Vehicle Power and Propulsion Conference (VPPC), 2010 IEEE*, sept. 2010, pp. 1 –6.

[20] H. Pollock, C. Pollock, R. Walter, and B. Gorti, "Low cost, high power density, flux switching machines and drives for power tools," in *Industry Applications Conference, 2003. 38th IAS Annual Meeting. Conference Record of the*, vol. 3, oct. 2003, pp. 1451 – 1457 vol.3.

[21] A. Zulu, B. Mecrow, and M. Armstrong, "A wound-field three-phase flux-switching synchronous motor with all excitation sources on the stator," *IEEE Trans. Ind. Appl.*, vol. 46, no. 6, pp. 2363 –2371, nov.-dec. 2010.

[22] Z. Zhu, Y. Pang, D. Howe, S. Iwasaki, R. Deodhar, and A. Pride, "Analysis of electromagnetic performance of flux-switching permanent-magnet machines by nonlinear adaptive lumped parameter magnetic circuit model," *IEEE Trans. Magn.*, vol. 41, no. 11, pp. 4277 – 4287, nov. 2005.

[23] Y. Chen, Z. Zhu, and D. Howe, "Three-dimensional lumped-parameter magnetic circuit analysis of single-phase flux-switching permanent-magnet motor," *IEEE Trans. Ind. Appl.*, vol. 44, no. 6, pp. 1701 –1710, nov.-dec. 2008.

[24] B. Gysen, E. Ilhan, K. Meessen, J. Paulides, and E. Lomonova, "Modeling of flux switching permanent magnet machines with fourier analysis," *IEEE Trans. Magn.*, vol. 46, no. 6, pp. 1499 –1502, june 2010.

[25] E. Ilhan, M. Kremers, E. Motoasca, J. Paulides, and E. Lomonova, "Spatial discretization methods for air gap permeance calculations in

$$C = \begin{bmatrix} 1&1&0&0&-1&-1&0&0&1&1&0&0&-1&1&0&0&1&1&0&0&-1&1&0&0&1&1&0&0&-1&1&0&0&1&1&0&0&-1&1&0&0 \\ 0&0&1&0&0&0&0&0&0&0&0&-1&0&0&1&0&0&0&0&0&0&0&0&-1&0&0&1&0&0&0&0&0&0&0&-1&0&0&1&0&0&0&0&-1 \\ 0&0&0&-1&0&0&1&0&0&0&0&0&0&0&0&-1&0&0&1&0&0&0&0&0&0&0&0&-1&0&0&1&0&0&0&0&0&0&0&-1&0&0&1&0&0&0 \\ 0&0&0&0&0&0&0&-1&0&0&1&0&0&0&0&0&0&0&0&-1&0&0&1&0&0&0&0&0&0&0&0&-1&0&0&1&0&0&0&0&0&0&0&-1&0&0&1&0 \end{bmatrix} \quad (65)$$

$$C = \begin{bmatrix} 1&1&0&0&0&0&0&-1&-1&0&0&0&0&0&1&1&0&0&0&0&0&-1&-1&0&0&0&0&0&1&1&0&0&0&0&0&-1&-1&0&0&0&0&0 \\ 0&0&1&1&0&0&0&0&0&0&0&0&0&0&0&0&-1&-1&0&0&1&1&0&0&0&0&0&0&0&0&0&0&0&-1&-1&0&0&0&0&0&0&0&0 \\ 0&0&0&0&-1&-1&0&0&1&1&0&0&0&0&0&0&0&0&0&0&0&0&-1&-1&0&0&1&1&0&0&0&0&0&0&0&0&0&0&0&-1&-1&0&0&1&1&0 \\ 0&0&0&0&0&0&0&0&0&0&-1&-1&0&0&1&1&0&0&0&0&0&0&0&0&0&0&0&0&-1&-1&0&0&1&1&0&0&0&0&0&0&0&0&-1&-1&0&0 \end{bmatrix} \quad (66)$$

double salient traction motors," *IEEE Trans. Ind. Appl.*, vol. 48, no. 6, pp. 2165–2172, Nov.-Dec.
[26] E. Ilhan, J. Paulides, L. Encica, and E. Lomonova, "Tooth contour method implementation for the flux-switching pm machines," in *Electrical Machines (ICEM), 2010 XIX International Conference on*, Sept., pp. 1–6.
[27] B. Gaussens, E. Hoang, O. de la Barriere, J. Saint-Michel, M. Lecrivain, and M. Gabsi, "Analytical approach for air-gap modeling of field-excited flux-switching machine: No-load operation," *IEEE Trans. Magn.*, vol. 48, no. 9, pp. 2505 –2517, sept. 2012.
[28] Z. Zhu and D. Howe, "Instantaneous magnetic field distribution in brushless permanent magnet dc motors. iii. effect of stator slotting," *IEEE Trans. Magn.*, vol. 29, no. 1, pp. 143 –151, jan 1993.
[29] ——, "Instantaneous magnetic field distribution in permanent magnet brushless dc motors. iv. magnetic field on load," *IEEE Trans. Magn.*, vol. 29, no. 1, pp. 152 –158, jan 1993.
[30] D. Zarko, D. Ban, and T. Lipo, "Analytical calculation of magnetic field distribution in the slotted air gap of a surface permanent-magnet motor using complex relative air-gap permeance," *IEEE Trans. Magn.*, vol. 42, no. 7, pp. 1828 – 1837, july 2006.
[31] ——, "Analytical solution for cogging torque in surface permanent-magnet motors using conformal mapping," *IEEE Trans. Magn.*, vol. 44, no. 1, pp. 52 –65, jan. 2008.
[32] T. Lubin, T. Hamiti, H. Razik, and A. Rezzoug, "Comparison between finite-element analysis and winding function theory for inductances and torque calculation of a synchronous reluctance machine," *IEEE Trans. Magn.*, vol. 43, no. 8, pp. 3406 –3410, aug. 2007.
[33] U. Kim and D. Lieu, "Magnetic field calculation in permanent magnet motors with rotor eccentricity: with slotting effect considered," *IEEE Trans. Magn.*, vol. 34, no. 4, pp. 2253 –2266, jul 1998.
[34] G. Dajaku and D. Gerling, "Stator slotting effect on the magnetic field distribution of salient pole synchronous permanent-magnet machines," *IEEE Trans. Magn.*, vol. 46, no. 9, pp. 3676 –3683, sept. 2010.
[35] S. Sadeghi and L. Parsa, "Multiobjective design optimization of five-phase halbach array permanent-magnet machine," *IEEE Trans. Magn.*, vol. 47, no. 6, pp. 1658 –1666, june 2011.
[36] B. Gaussens, E. HOANG, O. de la Barriere, J. Saint-Michel, P. MANFE, M. LECRIVAIN, and M. Gabsi, "Analytical armature reaction field prediction in field-excited flux-switching machines using an exact relative permeance function," *IEEE Trans. Magn.*, vol. PP, no. 99, p. 1, 2012.
[37] Z. Zhu, L. Wu, and Z. Xia, "An accurate subdomain model for magnetic field computation in slotted surface-mounted permanent-magnet machines," *IEEE Trans. Magn.*, vol. 46, no. 4, pp. 1100 –1115, april 2010.
[38] T. Lubin, S. Mezani, and A. Rezzoug, "Exact analytical method for magnetic field computation in the air gap of cylindrical electrical machines considering slotting effects," *IEEE Trans. Magn.*, vol. 46, no. 4, pp. 1092 –1099, april 2010.
[39] Z. Liu and J. Li, "Analytical solution of air-gap field in permanent-magnet motors taking into account the effect of pole transition over slots," *IEEE Trans. Magn.*, vol. 43, no. 10, pp. 3872 –3883, oct. 2007.
[40] F. Dubas and C. Espanet, "Analytical solution of the magnetic field in permanent-magnet motors taking into account slotting effect: No-load vector potential and flux density calculation," *IEEE Trans. Magn.*, vol. 45, no. 5, pp. 2097 –2109, may 2009.
[41] H. Tiegna, A. Bellara, Y. Amara, and G. Barakat, "Analytical modeling of the open-circuit magnetic field in axial flux permanent magnet machines with semi-closed slots," *IEEE Trans. Magn.*, vol. PP, no. 99, p. 1, 2011.
[42] O. de la Barriere, H. Ben Ahmed, M. Gabsi, and M. LoBue, "2d analytical airgap field model of an inset permanent magnet synchronous machine, taking into account the slotting effect," *IEEE Trans. Magn.*, vol. PP, no. 99, p. 1, 2012.
[43] J. Chen, Z. Zhu, S. Iwasaki, and R. Deodhar, "A novel e-core switched-flux pm brushless ac machine," *IEEE Trans. Ind. Appl.*, vol. 47, no. 3, pp. 1273 –1282, may-june 2011.
[44] M. Cheng, Y. Fan, and K. T. Chau, "Design and analysis of a novel stator doubly-fed doubly salient motor for electric vehicles," *Journal of Applied Physics*, vol. 97, no. 10, pp. 10Q508 –10Q508–3, may 2005.

Gaussens Benjamin was born in Toulouse, France, in 1987. He received the M.Sc. degree in electrical engineering from the Institut National Polytechnique (ENSEEIHT), Toulouse, France. He is currently working toward the Ph.D. degree still in electrical engineering at SATIE, ENS Cachan, CNRS, UniverSud. His current research interests include design of innovative topology of electromagnetic actuators and their modeling.

De la Barrière Olivier was born in Paris, France, in 1982. He received the M.Sc. degree in electronics from the Ecole Nationale Superieure de l'Electronique et de ses Applications (ENSEA), and the Ph.D. degree in electrical engineering from the Ecole Normale Supérieure de Cachan. He is now a Reseacher at SATIE, ENS Cachan, CNRS, UniverSud. His research topics include analytical modelling of electrical actuators, and also the study of new magnetic materials for electrical engineering applications.

Hoang Emmanuel was born in Antibes, France, in 1966. He received the "agrégation" in electrical engineering in 1990 and the Ph.D. degree from the Ecole Normale Supérieure de Cachan in 1995. Since 1990, he has worked with the electrical machine team in the SATIE laboratory. His research interests include the modeling of the iron losses in SRMs and the design, modeling, optimization, and control of novel topologies of PM machines.

Saint-Michel Jacques was born in 1949. He received the degree in engineering from Ecole Centrale de Paris, Paris, France, in 1972, and the Ph.D. degree from the University of Paris VI, Paris. From 1972 to 1982, he was with the French National Scientific Research Center (CNRS). In 1982, he joined Jeumont Schneider as the Head of the Design and Planning Department and remained with them until 1990. In 1990, he joined Leroy-Somer Motor, Angoulême, France, as a Technical Manager, becoming Scientific Director in 1998.

Manfe Philippe was born in 1957. He received the degree in engineering from Ecole Nationale Supérieure d'Electricité et de Mécanique, and the Ph.D. degree from the Institut National Polytechnique de Lorraine, Nancy, France. From 1981 to 1984, he was with the French National Scientific Research Center (CNRS). In 1985, he joined Leroy Somer Motors and Drive Division, Angoulême, France to Design and Develop high performance motors and drives for industrial and automotive markets. In 1997 he joined the Alternators Division as Electrical Engineering Manager, and is currently Engineering Director for LV Generators in Emerson/LS Electric Power Generation Division.

Lécrivain Michel was born in Barneville, France. He received the degree in electrical engineering from the Conservatoire National des Arts et Métiers (CNAM, Paris, France) in 1981. In 1997 he joined SATIE laboratory as a Research Engineer. His research interests include the design and control of new hybrid machines and novel permanent-magnet machines for automotive applications.

Gabsi Mohamed received the Ph.D. degree in electrical engineering from University of Paris-VI in 1987 and the HDR in 1999 from University of Paris-XI (Orsay, France). Since 1990, he has been working with the electrical machine team (SETE, Systèmes d'Energies pour le Transport et l'Environnement) of SATIE laboratory where he is currently a Full Professor and the Director of the Electrical Engineering Department. His research interests include SRM, vibrations and acoustic noise, and PM machines.